



OPEN

Superior Field Emission Properties of Layered WS₂-RGO NanocompositesSUBJECT AREAS:
ELECTRONIC DEVICES
TWO-DIMENSIONAL
MATERIALSChandra Sekhar Rout¹, Padmashree D. Joshi², Ranjit V. Kashid², Dilip S. Joag², Mahendra A. More², Adam J. Simbeck³, Morris Washington³, Saroj K. Nayak^{1,3} & Dattatray J. Late⁴¹School of Basic Sciences, Indian Institute of Technology, Bhubaneswar 751013, India, ²Center for Advanced Studies in Material Science and Condensed Matter Physics, Department of Physics, University of Pune, Pune 411007, India, ³Department of Physics, Applied Physics, and Astronomy, Rensselaer Polytechnic Institute, Troy, New York 12180, USA, ⁴Physical & Materials Chemistry Division, CSIR-National Chemical Laboratory, Pashan Road, Pune 411008, India.Received
14 August 2013Accepted
24 October 2013Published
21 November 2013Correspondence and
requests for materials
should be addressed to
C.S.R. (csrout@iitbbs.
ac.in); S.K.N.
(nayaks@rpi.edu) or
D.J.L. (dj.late@ncl.res.
in)

We report here the field emission studies of a layered WS₂-RGO composite at the base pressure of $\sim 1 \times 10^{-8}$ mbar. The turn on field required to draw a field emission current density of $1 \mu\text{A}/\text{cm}^2$ is found to be 3.5, 2.3 and 2 V/ μm for WS₂, RGO and the WS₂-RGO composite respectively. The enhanced field emission behavior observed for the WS₂-RGO nanocomposite is attributed to a high field enhancement factor of 2978, which is associated with the surface protrusions of the single-to-few layer thick sheets of the nanocomposite. The highest current density of $\sim 800 \mu\text{A}/\text{cm}^2$ is drawn at an applied field of 4.1 V/ μm from a few layers of the WS₂-RGO nanocomposite. Furthermore, first-principles density functional calculations suggest that the enhanced field emission may also be due to an overlap of the electronic structures of WS₂ and RGO, where graphene-like states are dumped in the region of the WS₂ fundamental gap.

Following the graphene^{1–4} revolution, graphene analogues of other inorganic layered materials have received significant attention from the scientific community due to their interesting and useful properties as well as their direct applications in various nanoelectronic devices. Among all the layered compounds: MoS₂^{4–12}, MoSe₂^{13–16}, WS₂^{6,17,18}, WSe₂^{19–21}, GaS^{7,22,23}, GaSe^{7,22,24}, TaS₂^{25,26}, RhTe₂²⁷, PdTe₂²⁸ are semiconductors; h-BN^{29,30} and HfS₂³¹ are insulators; NbS₂³², NbSe₂³³, NbTe₂³⁴, and TaSe₂^{26,35,36} are superconductors; while Bi₂Te₃^{37,38} and Bi₂Se₃^{39,40} act as topological insulators with good thermoelectric properties.

Field electron emission is the extraction of electrons from conducting/semiconducting materials via tunneling through the surface potential barrier by applying a very strong electric field of the order of 10^6 – 10^7 V/cm. Field emission has technological applications in various micro/nano-electronic devices. There is a great interest in the development of field emission based cathodes using various 1-dimensional (1D) and 2-dimensional (2D) nanostructured materials. 1D and 2D materials such as carbon nanotubes (CNTs)^{41,42}, ZnO^{43–45}, LaB₆^{46–48}, graphene^{49,50}, reduced graphene oxide (RGO)⁵¹ and MoS₂⁵² have emerged as potential field emitter candidates. 2D materials are known for their atomically thin planar structure, which is already utilized in flat technology such as flat panel field emission displays. Amongst all 2D materials, graphene, GO and layered MoS₂ sheets have been recently explored by researchers for their field emission properties. Graphene analogues of other 2D layered materials have emerged in material science and nanotechnology due to the enriched physics and novel enhanced properties they present. There are several advantages of using 2D nanomaterials in field emission based devices, including a thickness of only a few atomic layers, high aspect ratio (the ratio of lateral size to sheet thickness), excellent electrical properties, extraordinary mechanical strength and ease of synthesis. Furthermore, the presence of edges can enhance the tunneling probability for the electrons in layered nanomaterials similar to that seen in nanotubes^{41,42}.

The inorganic chalcogenide material WS₂ is a naturally occurring tungstite compound formed by 2D covalently bonded S-W-S layers separated by a van der Waals gap. Weak van der Waals interactions also hold the adjacent sulphur sheets together with a layer sequence S-W-S^{6,17,18,53}. WS₂ possesses hexagonal crystal structure with space group *P63/mmc* and each WS₂ monolayer contains an individual layer of W atoms with 6-fold coordination symmetry, which are then hexagonally packed between two trigonal atomic layers of S atoms^{6,17,18,53}. The WS₂ material has attracted attention for diverse applications in future nanoelectronic devices because of its 2D layered structure and direct-band gap^{6,17,18}. Whereas bulk WS₂ has an indirect band gap of 1.35 eV, when it is thinned to a single layer it becomes direct band gap semiconductor with a gap of 2.05 eV^{17,18}.

We have recently reported field emission properties of layered MoS₂ sheets exhibiting a turn on field of 3.5 V/ μm to draw a current density of $10 \mu\text{A}/\text{cm}^2$ ⁵². This has generated interest in field emission studies of other



transition metal dichalcogenides such as WS_2 . Furthermore, in an attempt to enhance the field emission properties of WS_2 , we have prepared a composite of WS_2 on RGO by a low-temperature hydrothermal method. We report here for the first time field emission studies on a layered WS_2 and WS_2 -RGO nanocomposite, where the RGO supported system exhibits superior field emission. We relate this superior performance to enhanced electric fields at the sheet edges and surface protrusions in the WS_2 -RGO composite. In addition, first-principles density functional theory (DFT) calculations show that the enhanced emission may also be due in part to the overlapping nature of the electronic structure of the composite system.

Results

Fig. 1 shows a field emission scanning electron microscope (FE-SEM) image of single-layer to a few-layered WS_2 sheets (Fig. 1a) and WS_2 -RGO nanocomposite sheets deposited on a Si substrate (Fig. 1b). The FE-SEM images reveal that the thickness of stacked WS_2 sheets is $\sim 1\text{--}5\text{ nm}$ and their length is in the range of $\sim 1\text{--}3\text{ }\mu\text{m}$. These images also reveal that the Si substrate was completely covered with WS_2 sheets and that the sheets possess a rough morphology along with vertical alignment (see Fig. S1, Supplementary Information). The FE-SEM images of composite WS_2 -RGO exhibit a large number of protruding edges on the surface as compared to WS_2 and RGO sheets (see Supplementary Information, Fig. S1). Fig. 1c shows the typical X-Ray diffraction (XRD) pattern of WS_2 sheets and the WS_2 -RGO nanocomposite. XRD analysis of the WS_2 sheets and WS_2 -RGO nanocomposite shows high crystalline hexagonal structure [Powder diffraction file (PDF) no. 84-1398] without any other impurities. The XRD data of WS_2 sheets shows the direction of sheet growth is along the (002) direction. The XRD pattern of the WS_2 -RGO composite shows a broad (002) peak and a more intense (100) peak as compared to the WS_2 sheets. The broadness of the (002) peak indicates both smaller size and fewer layers for the WS_2 sheets. Also, it confirms the growth of a large number of

protrusion edges along the (100) direction on RGO. Raman spectroscopy reveals the characteristic peaks of WS_2 in the $200\text{--}500\text{ cm}^{-1}$ range and the D (1348 cm^{-1}) and G (1587 cm^{-1}) bands of RGO in the WS_2 -RGO composite (Fig. 1d). In both the WS_2 sheets and the WS_2 -RGO composite three bands are observed at 312 , 345 and 415 cm^{-1} which corresponds to the E_{1g} , E_{2g}^1 and A_{1g} modes, respectively^{54,55}.

Transmission Electron microscopy (TEM) analysis demonstrates the formation of single crystalline, few-layered WS_2 sheets (Fig. 2 and Supplementary Information, Fig. S2). The high-resolution Transmission Electron microscopy (HRTEM) image revealed stacking of WS_2 (002) layers with an Interplanar spacing of 0.62 nm and periodic arrays of (100) planes with a spacing of 0.27 nm (Fig. 2c). In the planar orientation, lattice fringes along (100) and (110) planes of the hexagonal WS_2 are clearly observed (Fig. 2c, d). Fig. 2e, f show TEM images of WS_2 -RGO sheets, which indicate uniform coverage of WS_2 on RGO. HRTEM analysis reveals epitaxial growth of thin layered, hexagonal WS_2 on RGO (Fig. 2g, h and Supplementary Information S3). HRTEM analysis near the edge of the WS_2 sheets shows an interlayer spacing of $\sim 0.34\text{ nm}$, which confirms the growth of WS_2 from that of the graphene sheet (Fig. 2c and Supplementary Information, Fig. S3). Since GO sheets exhibit enormously active edges and functional groups on their basal plane, they act as a novel substrate for the nucleation and subsequent growth of WS_2 . Hence during hydrothermal reaction with a GO solution, the tungsten precursor was reduced to form WS_2 on GO and GO transformed to RGO.

Discussion

As described above, the hybrid nanostructures of 2D materials can be controllably prepared by the simple hydrothermal method. The hybrid nanostructures consisting of two 2D materials have numerous sharp edges and a huge proportion of nano-protrusions. Due to the unique morphologies, the hybrid nanostructures should have enhanced field emission properties. For comparison, we also show the field emission properties of pure RGO and WS_2 sheets.

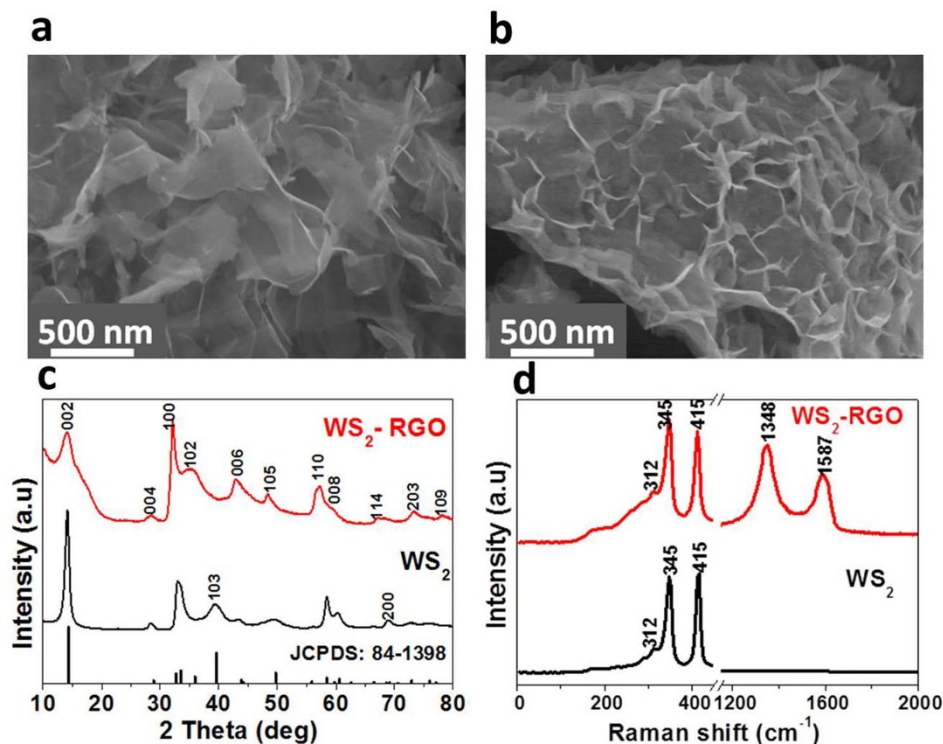


Figure 1 | Field emission scanning electron microscopy (FE-SEM) images of the (a) WS_2 and (b) WS_2 -RGO nanocomposite emitters. (c) XRD patterns of WS_2 sheets and WS_2 -RGO nanocomposite. (d) Raman spectra of WS_2 and WS_2 -RGO nanocomposite.

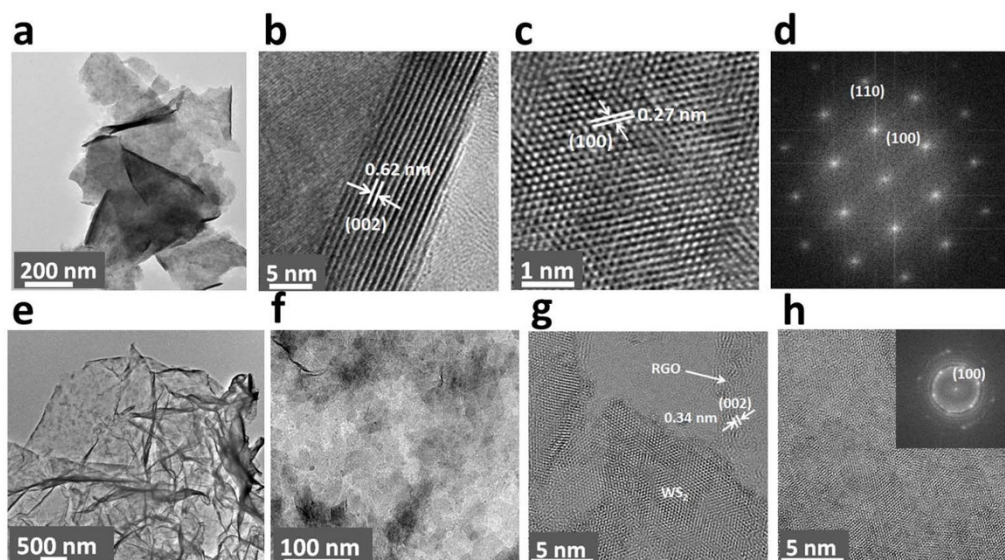


Figure 2 | TEM analysis of WS_2 sheets: (a) low magnification image, (b) high resolution image showing the multilayer nature of the sheets, (c) high resolution image of the sheets showing the hexagonal structure of WS_2 and (d) fast Fourier transform of the electron diffraction pattern of a few layers of WS_2 . TEM analysis of WS_2 -RGO sheets: (e, f) TEM images and (g, h) HRTEM images showing (002) lattice planes of RGO. Inset of (h) is a selected area for electron diffraction patterning of a few layers of WS_2 .

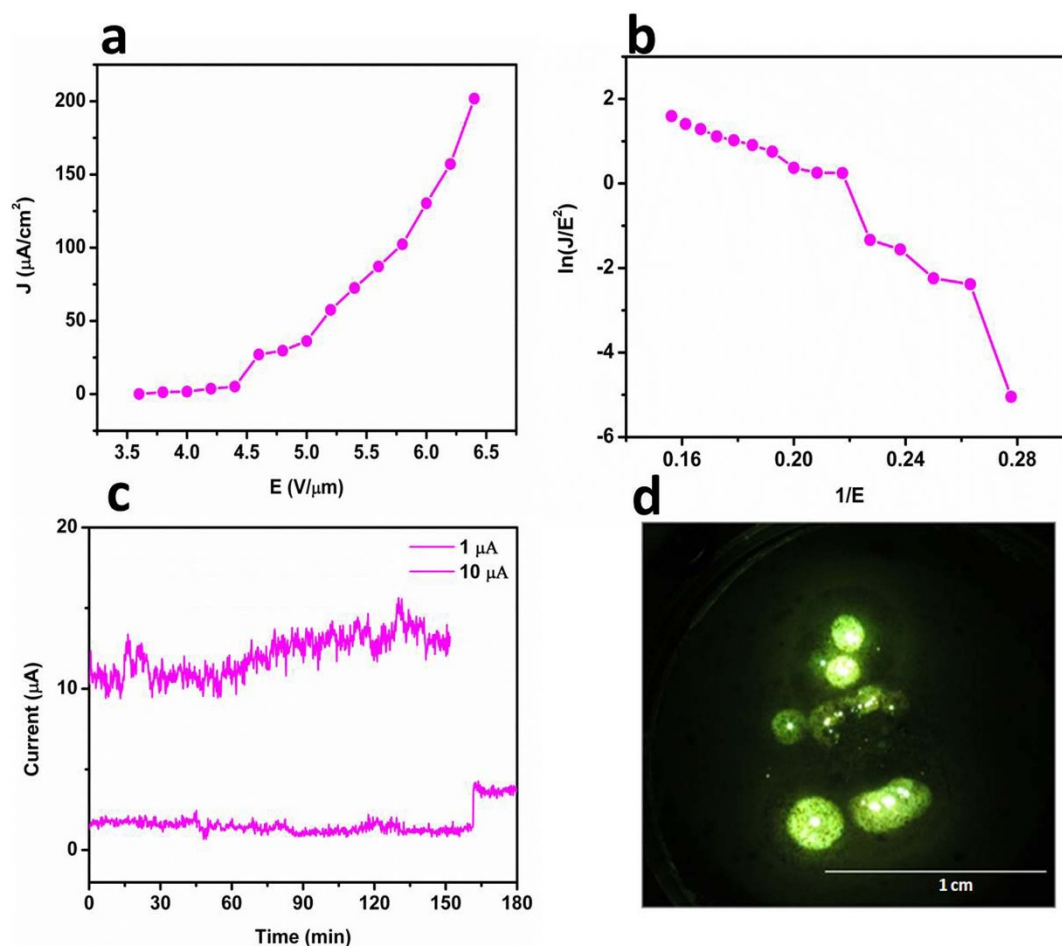


Figure 3 | Field emission from few-layered WS_2 sheets. (a) Applied electrical field as a function of emission current density. (b) F-N plot showing non-linear behaviour indicating emission current from the semiconducting emitter. (c) Long term field emission current stability indicating fairly stable emission current. (d) Field emission pattern taken during the long term stability study of the emitter.

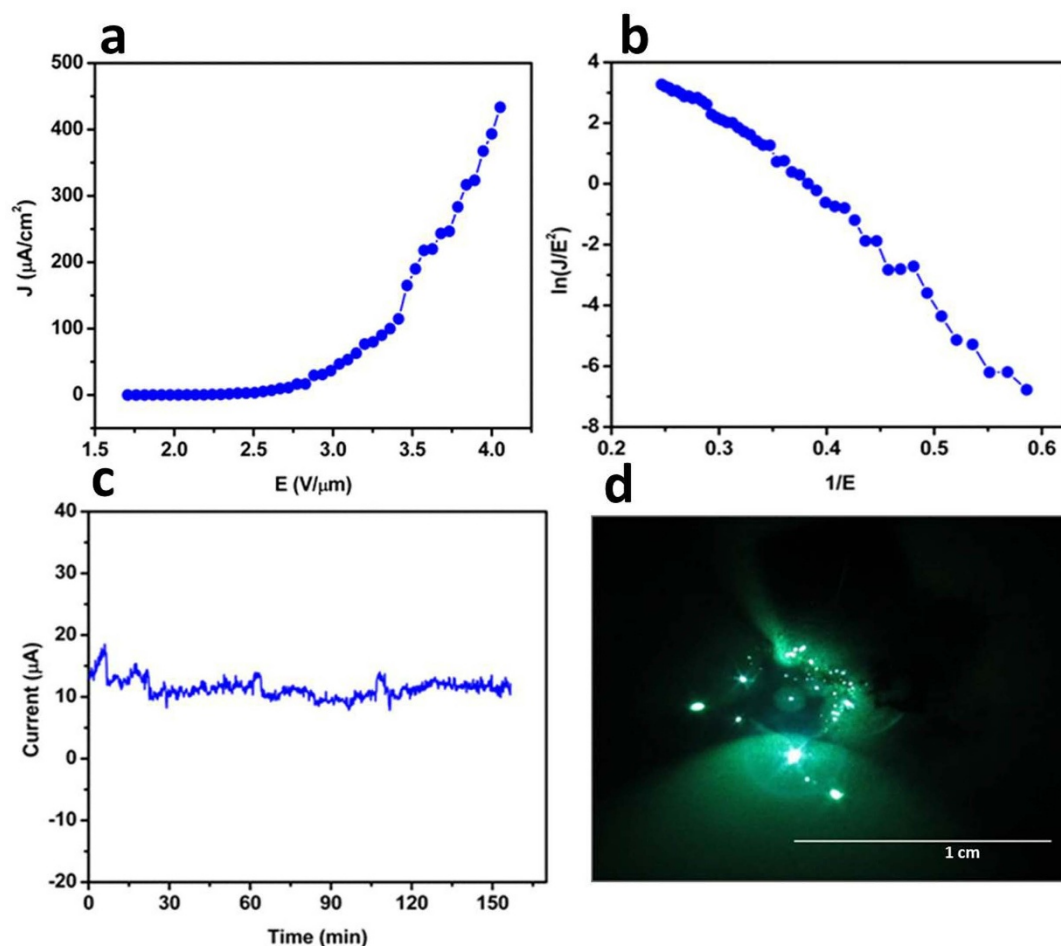


Figure 4 | Field emission from RGO sheets. (a) Applied electrical field as a function of emission current density. (b) F-N plot showing linear behaviour indicating emission current from the metallic emitter. (c) Long term field emission current stability (at 10 μA) indicating fairly stable emission current. (d) Field emission pattern taken during the long term stability study of the emitter.

The Fowler-Nordehim (F-N) equation for field emitters deposited on flat substrates has been suitably modified to yield an equation in terms of current density (J) and the applied electric field ($E = V/d$, where V is the voltage applied between the flat cathode and the anode screen, and d is their separation). The modified F-N equation is as follows^{56,57},

$$J = a\phi^{-1}E^2\beta^2 \exp\left(-\frac{b\phi^{\frac{3}{2}}}{\beta E}\right) \quad (1)$$

where a and b are constants ($a = 1.54 \times 10^{-6} \text{ AeV V}^{-2}$, $b = 6.83 \text{ eV}^{-3/2} \text{ Vnm}^{-1}$), J is the current density, E is the local electric field (surface field) and β is the local electric field enhancement factor.

The plot of the field emission current density J versus applied electric field E for WS_2 is shown in Fig. 3a. The F-N plot [a plot of $\ln(J/E^2)$ versus $1/E$] for the WS_2 sheets is shown in Fig. 3b with a calculated field enhancement factor of ~ 1182 (calculated from slope of the linear region of F-N plot). The F-N plot for the WS_2 field emitter is nearly linear and shows a tendency for saturation at high electric fields. Fig. 3c shows the typical long term current stability from a WS_2 nanosheet field emitter. Fig. 3d shows the typical field emission micrograph of the WS_2 nanosheet field emitter recorded at a current density of $50 \mu\text{A}/\text{cm}^2$. The field emission from RGO sheets is shown in Fig. 4a as a function of applied electrical field versus emission current density. Fig. 4b shows the corresponding F-N plot showing linear behaviour. Fig. 4c shows the long term field emission current stability for RGO sheets, indicating a stable emission current.

Fig. 4d shows the field emission pattern for RGO sheets taken during long-term current stability measurements of the emitter.

Fig. 5a shows a J - E plot for the WS_2 -RGO nanocomposite. Fig. 5b depicts the corresponding F-N plot for the WS_2 -RGO nanocomposite with a field enhancement factor of 2994. Fig. 5c shows the long term current stability measurements for WS_2 -RGO nanocomposites. Fig. 5d shows the typical field emission micrograph of WS_2 -RGO sheets recorded at a current density $50 \mu\text{A}/\text{cm}^2$. The field emission micrograph of the WS_2 -RGO composite consists of a large number of tiny bright spots and more uniform emission as compared to the WS_2 and RGO field emitter.

The field enhancement factor can provide a quantitative idea of the degree of enhancement of the electric field at the emitter (WS_2 and WS_2 -RGO) sheet edges due to their nanometric dimension. In the present case, the field enhancement factor is calculated from the slope of the F-N plots using

$$\beta = \frac{-6.8 \times 10^3 \phi^{3/2}}{m} \quad (2)$$

where β represents the field enhancement factor, m is slope of F-N plot and ϕ is the workfunction of the emitter, which is determined from density functional theory (DFT) calculations to be 5.89 eV for WS_2 and 4.48 eV for RGO (see discussion below and Computational Methods section for details). The field enhancement factor values calculated from equation (2) are found to be 2468, 2619 and 2978 for WS_2 , RGO and the WS_2 -RGO nanocomposite field emitters, respectively. Table 1 in the Supplementary Information shows a comparison

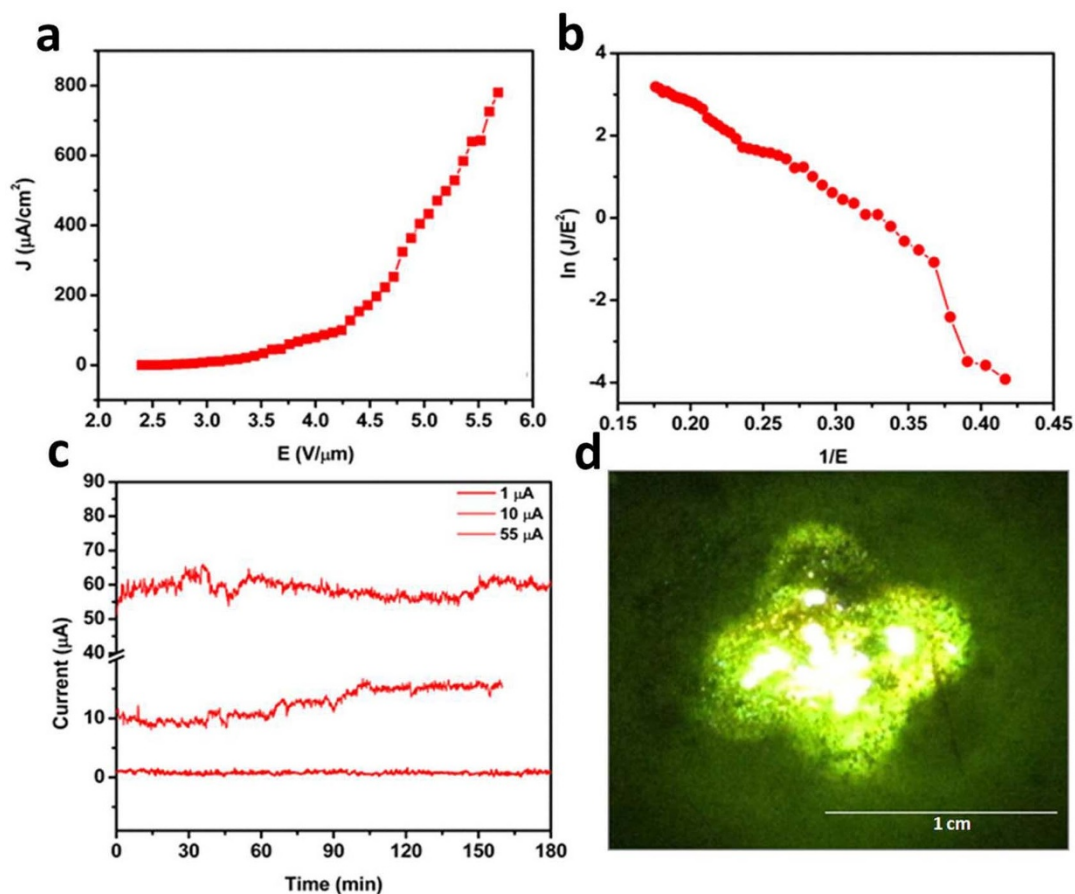


Figure 5 | Field emission studies of few-layered WS₂-RGO nanosheets. (a) Applied electric field vs. field emission current density. (b) F-N plot showing non-linear behaviour typical of the semiconducting emitter. (c) Long term field emission current stability at 1, 10 and 50 μA indicating fluctuations in stability due to adsorption and desorption of gas molecules. (d) Field emission pattern taken during the long term stability study of the emitter.

of electric field values required to draw an emission current density of 1 $\mu\text{A}/\text{cm}^2$, 10 $\mu\text{A}/\text{cm}^2$ and 100 $\mu\text{A}/\text{cm}^2$ (See. Supplementary Information). The observed turn on and threshold values for the WS₂-RGO nanocomposite are significantly lower than that of the few-layered WS₂ field emitter. The low turn on values in the case of WS₂-RGO are attributed to the atomically sharp edges of the WS₂-RGO nanocomposite sheets, which are reflected by the high value of the field enhancement factor as compared to the WS₂ field emitter. This can be explained on the basis of FE-SEM imaging which shows a higher concentration of protruding edges in the case of the WS₂-RGO composite than in case of WS₂ sheets. Also, the observed field emission image for WS₂-RGO clearly depicts a higher density of emission spots for the emitter, corroborating with the estimated values of β as explained above. Furthermore, the DFT calculations show that in addition to the surface protrusions and edge effects, the enhanced field emission may also be partly attributed to the overlapping electronic structure of the composite.

The geometry of the composite system is featured in Fig. 6a, b. As mentioned in the Computational Methods section, for simplicity, the composite system is taken as WS₂ atop graphene, and in order to match the two lattices the strain is shared between the two monolayers. The strained WS₂ lattice constant is taken as 3.09 Å (−1.18%) and graphene as 2.48 Å (+1.21%). Here we have defined the strain relative to the theoretically predicted lattice constants. This relatively small amount of strain has minor effects on the geometry and electronic structure of WS₂ and graphene. For example, optimization of the pristine WS₂ unit cell yields bond lengths of W-S = 2.39 Å and S-S = 3.12 Å, in agreement with ref. 58, whereas in the strained cell W-S = 2.38 Å and S-S = 3.15 Å. Quadrupling (Quintupling) the WS₂

(graphene) lattice then gives the supercell lattice constant of 12.37 Å for the composite system. To combine the two monolayers, WS₂ is simply placed atop graphene at a separation of 3.33 Å (Fig. 6b). Note that rotational and other lattice mismatch effects have not been considered in this work, and are not suspected to alter the conclusions.

From our self-consistent energy calculations the work function ϕ of the free-standing systems can be calculated using

$$\phi = E_{\text{vac}} - E_F \quad (3)$$

where E_{vac} is the converged electrostatic potential in the vacuum region and E_F is the Fermi energy. The work functions of strained WS₂ ϕ_{WS_2} and graphene ϕ_G are computed using Equation 3. Our methodology is verified by the calculation of the work function for pristine graphene $\phi_G = 4.48$ eV, which is in perfect agreement with ref. 59. For the strained WS₂ monolayer it is found that $\phi_{\text{WS}_2} = 5.89$ eV, whereas for strained graphene the work function, compared to WS₂, is predicted to be significantly smaller: $\phi_G = 4.58$ eV. The change in the respective work functions when the composite is formed is negligible.

The projected density of states (PDOS) analysis is featured in Fig. 6c, where only the states which give major contributions to the bands near the Fermi energy are shown, i.e. W *d*-states, S *p*-states, and C *p*-states (Fig. 6c, left, middle, and right, respectively). Note that for the freestanding WS₂ system the DOS has been centered on the band gap, whereas for the composite system the Fermi energy is determined by graphene. The presence of the graphene substrate essentially has no appreciable effect on the WS₂ DOS, and vice-versa,

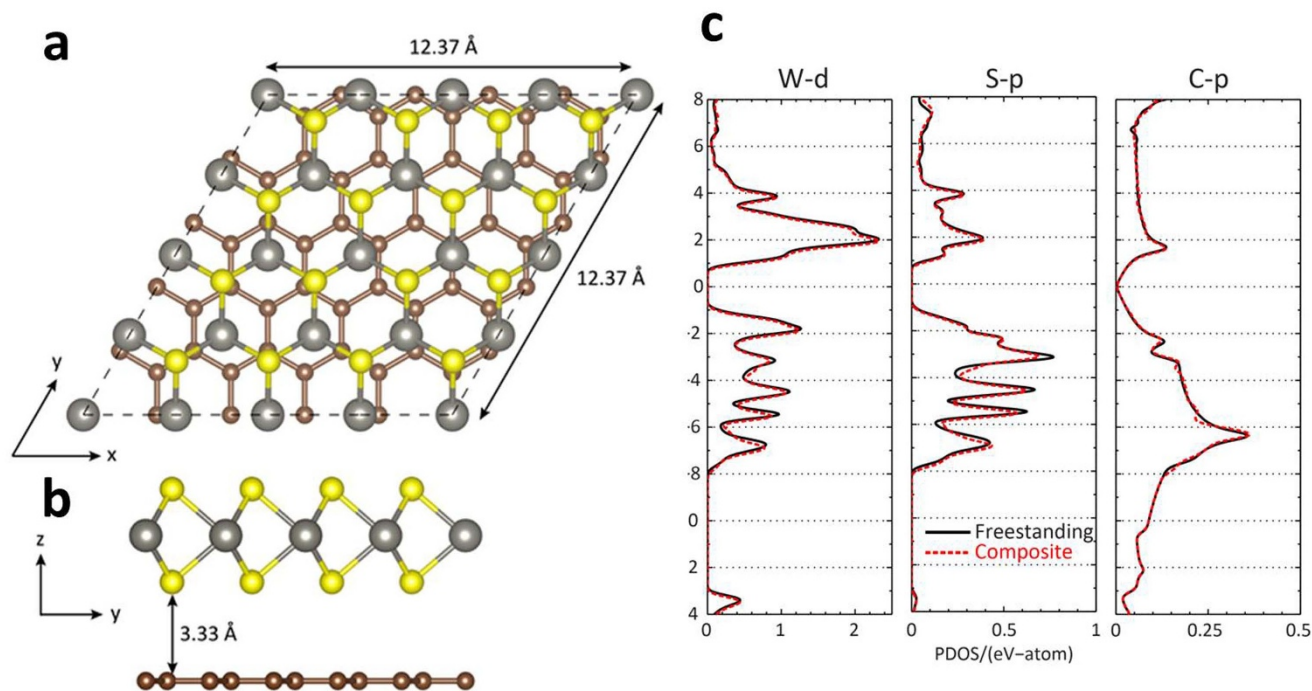


Figure 6 | (a) Top and (b) side views of the composite WS₂-graphene system. The system contains a total of 98 atoms: 32 S (yellow/light), 16 W (grey), and 50 C (brown/dark). The lattice mismatch between the two monolayers has been treated by straining both WS₂ and graphene. (c) Select partial density of states (PDOS) of freestanding (black, solid) and composite (red/grey, dashed) systems. From left to right: W *d*-states, S *p*-states, and C *p*-states. The presence of the graphene substrate leaves the WS₂ states intact while adding states in the WS₂ fundamental gap region. The zero of energy for the free standing WS₂ monolayer has been taken as half the band gap.

besides dumping states in the band gap region of WS₂. This addition of states, combined with the unappreciable change in work function, suggests that the composite system takes advantage of the *best of both worlds* in terms of the field emission properties of WS₂ and graphene. When an electric field is applied to the system electrons will first be removed from states nearest the Fermi energy, which in the composite system are due to graphene. Although the DOS is very low near E_F for graphene the work function is small, compared to WS₂, so that electrons are able to escape at a lower applied field. Eventually though, after continually increasing the bias, electrons will be also be emitted by WS₂. The work function of WS₂ is larger than that of graphene, by 1.31 eV, but now the DOS has dramatically increased and there are more electrons available for emission. Therefore the combined effect of the relative DOS and relative work functions of WS₂ and graphene also may play a role in the experimentally observed enhanced field emission.

In addition to increased performance, the applications of field emitters also require emission current stability, so it is a decisive and important parameter in the fabrication of field emission based nanoelectronic devices. Fig. 3c and Fig. 5c show the field emission current stability traces for WS₂ and the WS₂-RGO nanocomposite field emitters at different preset values for a sampling interval of 10 seconds recorded over a period of 3 hours. It has been observed that both WS₂ and WS₂-RGO show *spike* type fluctuations in the field emission current. The main cause of these *spike*-like fluctuations in emission current is adsorption/desorption and ion bombardment due to residual gas molecules⁸. Thus, during adsorption/desorption events the local work function varies slightly, depending upon the nature of the molecule (either electropositive or electronegative), on the emitter surface. The ion bombardment with residual gas molecules due to the presence of high electrostatic fields results in mechanical damage, further causing creation and destruction of emission sites, which in turn causes the fluctuations in the field emission current.

In summary, the field emission properties of WS₂ and WS₂-RGO have been investigated at the base pressure of $\sim 1 \times 10^{-8}$ mbar. The turn on field required to draw a current density of 1 $\mu\text{A}/\text{cm}^2$ is found to be 3.5 V/ μm and 2 V/ μm for WS₂ and the WS₂-RGO composite, respectively. Enhanced field emission behavior is observed for WS₂-RGO due to a high field enhancement factor associated with surface protrusions. In addition, the DFT results show that the enhanced field emission may be compounded by the overlapping electronic structures of WS₂ and RGO. Owing to the low turn on field and planar (sheet-like) structure morphology, the WS₂-RGO emitter can be utilized for new generation vacuum microelectronics/nanoelectronics and flat panel display applications.

Methods

The preparation of few layered WS₂ sheets. WS₂ sheets were synthesized by a one-step hydrothermal reaction. In a typical experiment, 3 mM WCl₆ (Sigma-aldrich, 99.98%) and 15 mM thioacetamide (C₂H₅NS, Sigma-Aldrich, $\geq 99\%$) were dissolved in 40 mL DI water and stirred for 1 hour at room temperature by using a magnetic stirrer. The solution was transferred to a 50 mL stainless steel autoclave, heated up to 265°C and kept for 24 hours. After cooling naturally, the product was filtered, washed with DI water and dried in vacuum at 60°C for 6 hours.

The preparation of WS₂-RGO composite. The WS₂-RGO composite was synthesized by the same hydrothermal reaction condition as that for WS₂ sheets. 8 mL of 5 mg/mL GO solution (see Supplementary Information) was added to the mixture of WCl₆ and thioacetamide and the total volume of the solution was maintained at 40 mL. The same processes mentioned for WS₂ sheets were followed. During the hydrothermal process, smaller size WS₂ sheets were epitaxially formed on GO and subsequently GO transformed to RGO (see Supplementary Information, Scheme 1). Carbon content in the final product was 3 wt%, which was confirmed by elemental analysis.

Materials characterization. The samples were characterized with X-ray diffraction equipped with the following: Ni filtered Cu K α radiation (40 kV, 100 mA, $\lambda = 0.15418$ nm), field emission scanning electron microscopy and high resolution transmission electron microscopy. The samples were also characterized by a Micro Raman spectrometer with a laser excitation wavelength of 532 nm.



Field emission. The field emission studies of few-layered WS₂/Si, RGO/Si and WS₂-RGO/Si nanocomposite were investigated independently in an ultra high vacuum (UHV) chamber at the base pressure of $\sim 1 \times 10^{-8}$ mbar. The UHV chamber is equipped with a rotary backed turbo molecular pump, sputter ion pump and titanium sublimation pump. For achieving base pressure of $\sim 1 \times 10^{-8}$ mbar, the chamber was baked at 200 °C for 12 hours. The field emission studies were carried out in close proximity setup, which was mounted in the UHV chamber. The close proximity setup consisted of specimens (WS₂/Si, WS₂-RGO/Si independently) acting as the cathode and a copper rod as the anode. Inter-electrode separation could be varied from 500 μ m to 1500 μ m using an insulating alumina spacer. The field emission current (I) versus applied voltage (V) was measured using Keithley 6514 electrometer and Spellman high voltage DC power supply. The field emission current stability was investigated using a computer controlled data acquisition system with a sampling interval of 10 seconds. The field emission micrographs were seen on a transparent ITO coated glass with a phosphor screen (anode) and were recorded using a digital camera (Canon SX150IS).

Computational methods. To model the WS₂-RGO system we consider the composite system of a monolayer of WS₂ deposited on graphene (Fig. 6a, b) within first-principles density functional theory (DFT). The DFT based Vienna *ab initio* simulation package (VASP)^{60–63} was employed with projector-augmented wave (PAW) pseudopotentials^{64,65} to describe the electron-ion interaction. The exchange-correlation energy is described using the local density approximation (LDA)⁶⁶ and it was found that the generalized gradient approximation (GGA)^{67,68} produces similar results. In order to match the WS₂ lattice to that of graphene, both monolayers are strained between 1–2%. To begin, the strained unit cell geometries are optimized until the forces on each atom are less than 0.01 eV/Å. For WS₂ (graphene), a plane-wave basis energy cutoff of 400 eV (600 eV), a $12 \times 12 \times 1$ ($18 \times 18 \times 1$) Monkhorst-Pack k-point sampling⁶⁹, and at least 12.5 Å (10 Å) of vacuum is necessary to see convergence in the total energy on the order of 1 meV per atom for the strained unit cells. Next, the strained unit cells are expanded and combined to form the composite supercell: WS₂ by 4× and graphene by 5× for a total of 98 atoms (32 S, 16 W, and 50 C). WS₂ is placed atop graphene at a fixed distance of 3.33 Å (Fig. 6b), representative of the van der Waals interaction between the two monolayers. Note that any further optimization of the geometry of the supercell does not affect the reported results. The strained supercell for the composite system employs similar parameters, except the k-point sampling is reduced to $6 \times 6 \times 1$. The energy of both the unit/supercell is relaxed until differences in total energy are less than 10^{-4} eV and Gaussian smearing with a width of 0.05 eV is used to describe the partial occupancies of the orbitals. From our self-consistent energy calculations the work function ϕ of the free-standing systems can be calculated using Equation (3) above. Note that in order for the electrostatic potential to converge smoothly in the vacuum region for the composite system, dipole corrections must be included to treat the dipole interactions which arise between periodic images in the asymmetric slab model⁷⁰. Finally, the results are also accompanied by a partial density of states (PDOS) analysis for the dominant states near the Fermi energy (Fig. 6c) in order to interpret the field emission properties of WS₂-RGO.

1. Geim, A. K. Graphene: Status and prospects. *Science* **324**, 1530–1534 (2009).
2. Novoselov, K. S. *et al.* Two-dimensional atomic crystals. *Proc. Nat. Acad. Sci. USA* **102**, 10451–10453 (2005).
3. Novoselov, K. S. *et al.* Electric field effect in atomically thin carbon films. *Science* **306**, 666–669 (2004).
4. Rao, C. N. R., Sood, A. K., Subrahmanyam, K. S. & Govindaraj, A. Graphene: the new two-dimensional nanomaterial. *Angew. Chem. Int. Ed.* **48**, 7752–7777 (2009).
5. Radisavljevic, B., Radenovic, A., Brivio, J., Giacometti, V. & Kis, A. Single-layer MoS₂ transistors. *Nature Nanotech.* **6**, 147–150 (2011).
6. Matte, H. S. S. R. *et al.* MoS₂ and WS₂ analogues of graphene. *Angew. Chem. Int. Ed.* **122**, 4153–4156 (2010).
7. Late, D. J., Liu, B., Matte, H. S. S. R., Rao, C. N. R. & Dravid, V. P. Rapid characterization of ultrathin layers of chalcogenides on SiO₂/Si substrates. *Adv. Func. Mater.* **22**, 1894–1905 (2012).
8. Late, D. J. *et al.* Hysteresis in single-layer MoS₂ field effect transistors. *ACS Nano* **6**, 5635–5641 (2012).
9. Late, D. J. *et al.* Sensing behavior of atomically thin-layered MoS₂ transistors. *ACS Nano* **7**, 4879–4891 (2013).
10. Jariwala, D. *et al.* Band-like transport in high mobility unencapsulated single-layer MoS₂ transistors. *Appl. Phys. Lett.* **102**, 173107 (2013).
11. Yin, Z. *et al.* Single-layered MoS₂ phototransistor. *ACS Nano* **6**, 74–80 (2012).
12. Li, H. *et al.* Fabrication of single-multilayer MoS₂ film-based field-effect transistors for sensing NO at room temperature. *Small* **8**, 63–67 (2012).
13. Tongay, S. *et al.* Thermally driven crossover from indirect toward direct bandgap in 2D semiconductors: MoSe₂ versus MoS₂. *Nano Lett.* **12**, 5576–5580 (2012).
14. Ross, J. S. *et al.* Electrical control of neutral and charged excitons in a monolayer semiconductor. *Nature Comm.* **4**, 1474, DOI: 10.1038/ncomms2498 (2013).
15. Larentis, S., Fallahazad, B. & Tutuc, E. Field-effect transistors and intrinsic mobility in ultra-thin MoSe₂ layers. *Appl. Phys. Lett.* **101**, 223104 (1–4) (2013).
16. Kong, D. *et al.* Synthesis of MoS₂ and MoSe₂ Films with vertically aligned layers. *Nano Lett.* **13**, 1341–1347 (2013).

17. Braga, D., Lezama, I. G., Berger, H. & Morpurgo, A. F. Quantitative determination of the band Gap of WS₂ with ambipolar Ionic Liquid-gated transistors. *Nano Lett.* **12**, 5218–5223 (2012).
18. Georgiou, T. *et al.* Vertical field-effect transistor based on graphene-WS₂ heterostructures for flexible and transparent electronics. *Nature Nanotech.* **8**, 100–103 (2013).
19. Fang, H. *et al.* High-performance single layered WSe₂ p-FETs with chemically doped contacts. *Nano Lett.* **12**, 3788–3792 (2012).
20. Liu, W. *et al.* Role of metal contacts in designing high-performance monolayer n-Type WSe₂ field effect transistors. *Nano Lett.* **13**, 1983–1990 (2013).
21. Zhao, W. *et al.* Evolution of electronic structure in atomically thin sheets of WS₂ and WSe₂. *ACS Nano* **7**, 791–797 (2013).
22. Late, D. J. *et al.* GaS and GaSe ultrathin layer transistors. *Adv. Mater.* **24**, 3549 (2012).
23. Hu, P. *et al.* Highly Responsive Ultrathin GaS Nanosheet Photodetectors on Rigid and Flexible Substrates. *Nano Lett.* **13**, 1649–1654 (2013).
24. Hu, P., Wen, Z., Wang, L., Tan, P. & Xiao, K. Synthesis of few-layer GaSe nanosheets for high performance photodetectors. *ACS Nano* **7**, 5988–5994 (2012).
25. Sipos, B., Kusmartseva, A. F., Berger, A. H., Forró, L. & Tutis, E. From Mott state to superconductivity in 1T-TaS₂. *Nature Mater.* **7**, 96–965 (2008).
26. Li, H. *et al.* Mechanical Exfoliation and Characterization of Single- and Few-Layer Nanosheets of WSe₂, TaS₂, and TaSe₂. *Small* **9**, 1974–1981 (2013).
27. Geller, S. J. *Am. Chem. Soc. The crystal structures of RhTe and RhTe₂*, 77, 2641–2644 (1955).
28. Jan, J. P. & Skriver, H. L. Relativistic bandstructure and Fermi surface of PdTe₂ by the LMTO method. *J. Phys. F: Met. Phys.* **7**, 1719–1730 (1977).
29. Gorbachev, R. V. *et al.* Hunting for monolayer Boron Nitride: Optical and Raman signatures. *Small* **7**, 465–468 (2011).
30. Kim, K. K. *et al.* Synthesis and characterization of hexagonal boron nitride film as a dielectric layer for graphene devices. *ACS Nano* **6**, 8583–8590 (2012).
31. Kreis, C., Werth, S., Adelung, R., Kipp, L. & Skibowski, M. Valence and conduction band states of HfS₂: From bulk to a single layer. *Phys. Rev. B* **68**, 235331 (1–6) (2003).
32. Liu, C. & Frindt, R. F. Anisotropic optical-absorption studies of NbS₂ single-layer suspensions aligned in a magnetic field. *Phys. Rev. B* **31**, 4086–4088 (1985).
33. Ayari, A., Cobas, E., Ogundadegbe, O. & Fuhrer, M. S. Realization and electrical characterization of ultrathin crystals of layered transition-metal dichalcogenides. *J. Appl. Phys.* **101**, 014507 (1–5) (2007).
34. Brown, B. E. The crystal structures of NbT₂ and TaT₂. *Acta Cryst.* **20**, 264–267 (1966).
35. Castellanos-Gomez, A. *et al.* Fast and reliable identification of atomically thin layers of TaSe₂ crystals. *Nano Research* DOI:10.1007/s12274-013-0295-9 (2013).
36. Galvis, J. A. *et al.* Scanning tunneling measurements of layers of superconducting 2H-TaSe₂: Evidence for a zero-bias anomaly in single layers. *Phys. Rev. B* **87**, 094502 (1–9) (2013).
37. Teweldebrhan, D., Goyal, V. & Balandin, A. A. Exfoliation and characterization of bismuth telluride atomic quintuples and quasi-two dimensional crystals. *Nano Lett.* **10**, 1209–1218 (2010).
38. Teweldebrhan, D., Goyal, V., Rahman, M. & Balandin, A. A. Atomically-thin crystalline films and ribbons of bismuth telluride. *Appl. Phys. Lett.* **96**, 053107 (1–3) (2010).
39. Steinberg, H., Gardner, D. R., Lee, Y. S. & Jarillo-Herrero, P. Surface state transport and ambipolar electric field effect in Bi₂Se₃ nanodevices. *Nano Lett.* **10**, 5032–5036 (2010).
40. Xia, Y. *et al.* Observation of a large-gap topological-insulator class with a single Dirac cone on the surface. *Nat. Phys.* **5**, 398–402 (2009).
41. de Heer, W. A., Châtelain, A. & Ugarte, D. A carbon nanotube field-emission electron source. *Science* **270**, 1179–1180 (1995).
42. Sharma, R. B., Late, D. J., Joag, D. S., Govindaraj, A. & Rao, C. N. R. Field emission properties of boron and nitrogen doped carbon nanotubes. *Chem. Phys. Lett.* **428**, 102–108 (2006).
43. Banerjee, D., Jo, S. H. & Ren, Z. F. Enhanced Field Emission of ZnO Nanowires. *Adv. Mater.* **16**, 2028–2032 (2004).
44. Ramgir, N. S. *et al.* Ultralow threshold field emission from a single multipod structure of ZnO. *Appl. Phys. Lett.* **88**, 042107 (1–3) (2006).
45. Late, D. J. *et al.* Enhanced field emission from pulsed laser deposited ZnO thin films on Re and W. *Appl. Phys. A* **95**, 613–620 (2009).
46. Late, D. J. *et al.* Field emission studies on well adhered pulsed laser deposited LaB₆ on W tip. *Appl. Phys. Lett.* **89**, 123510 (1–3) (2006).
47. Late, D. J. *et al.* Some aspects of pulsed laser deposited nanocrystalline LaB₆ film: atomic force microscopy, constant force current imaging and field emission investigations. *Nanotechnology* **19**, 265605 (2008).
48. Late, D. J. *et al.* Synthesis of LaB₆ micro/nano structures using picosecond (Nd:YAG) laser and its field emission investigations. *Applied Physics A* **97**, 905–909 (2009).
49. Palnitkar, U. A. *et al.* Remarkably low turn-on field emission in undoped, nitrogen-doped, and boron-doped graphene. *Appl. Phys. Lett.* **97**, 063102 (1–3) (2010).
50. Santandrea, S. *et al.* Field emission from single and few-layer graphene flakes. *Appl. Phys. Lett.* **98**, 163109 (1–3) (2011).



51. Ye, D., Moussa, S., Ferguson, J. D., Baski, A. A. & Samy Ei-Shall, M. Highly efficient electron field emission from graphene oxide sheets supported by nickel nanotip arrays. *Nano Lett.* **12**, 1265–1268 (2012).
52. Kashid, R. V. *et al.* Enhanced field-emission behavior of layered MoS₂ sheets. *Small* **9**, 2730–2734 (2013).
53. Tenne, R., Margulis, L., Genut, M. & Hodes, G. Polyhedral and cylindrical structures of tungsten disulfide. *Nature* **360**, 444 (1992).
54. Verble, J. L. & Wieting, T. J. Lattice Mode Degeneracy in MoS₂ and Other Layer Compounds. *Phys. Rev. Lett.* **25**, 362–365 (1970).
55. Virsek, M., Jesih, A., Milosevic, I., Damnjanovic, M. & Remskar, M. Raman scattering of the MoS₂ and WS₂ single nanotubes. *Surface Science* **601**, 2868–2872 (2007).
56. [Fursey, G. (ed.)] Field emission in vacuum microelectronics. (Kluwer Academic/Plenum publishers, New York, 2005).
57. Fowler, R. H. & Nordheim, L. *Proceedings of the Royal Society of London*, Electron emission in intense electric field. **119**, 173–181 (1928).
58. Ding, Y. *et al.* First principles study of structural vibrational and electronic properties of graphene-like MX₂ (M = Mo, Nb, W, Ta; X = S, Se, Te) monolayers. *Physica B-Condensed Matter*. **406**, 2254–2260 (2011).
59. Giovannetti, G. *et al.* Doping Graphene with Metal Contacts. *Phys. Rev. Lett.* **101**, 026803 (1–4) (2008).
60. Kresse, G. & Furthmuller, J. Efficient iterative schemes for ab-initio total energy calculations using a plane-wave basis set. *Comput. Mater. Sci.* **6**, 15–50 (1996).
61. Kresse, G. & Furthmuller, J. Efficient iterative schemes for *ab initio* total-energy calculations using a plane-wave basis set. *Phys. Rev. B* **54**, 11169–11186 (1996).
62. Kresse, G. & Hafner, J. *Ab initio* molecular dynamics for liquid metals. *Phys. Rev. B* **47**, 558–561 (1993).
63. Kresse, G. & Hafner, J. *Ab initio* molecular-dynamics simulation of the liquid-metal–amorphous-semiconductor transition in germanium. *Phys. Rev. B* **49**, 14251–14269 (1994).
64. Blochl, P. E. Projector augmented-wave method. *Phys. Rev. B* **50**, 17953–17979 (1994).
65. Kresse, G. & Joubert, D. From ultrasoft pseudopotentials to the projector augmented-wave method. *Phys. Rev. B* **59**, 1758–1775 (1999).
66. Perdew, J. P. & Zunger, A. Self-interaction correction to density-functional approximations for many-electron systems. *Phys. Rev. B* **23**, 5048–5079 (1981).
67. Perdew, J. P. *et al.* Atoms, molecules, solids, and surfaces: Applications of the generalized gradient approximation for exchange and correlation. *Phys. Rev. B* **46**, 6671–6687 (1992).
68. Perdew, J. P. *et al.* Erratum: Atoms, molecules, solids, and surfaces: Applications of the generalized gradient approximation for exchange and correlation. *Phys. Rev. B* **48**, 4978–4978 (1993).
69. Monkhorst, H. J. & Pack, J. D. Special points for brillouin-zone integrations. *Phys. Rev. B* **13**, 5188–5192 (1976).
70. Neugebauer, J. & Scheffler, M. Adsorbate-substrate and adsorbate-adsorbate interactions of Na and K adlayers on Al(111). *Phys. Rev. B* **46**, 16067–16080 (1992).

Acknowledgments

Authors C.S. Rout and D.J. Late would like to thank DST for the Ramanujan fellowship and Prof. C.N.R. Rao (FRS), for support and encouragement. P.D.J. would like to thank UGC for fellowship. D.S.J. and R.V.K. would like to thank CSIR (Government of India) for Emeritus Scientist Scheme and SRF respectively. This work is supported by the Interconnect Focus Center (MARCO program), State of New York; the National Science Foundation (NSF) Integrative Graduate Education and Research Traineeship (IGERT) program, Grant No. 0333314; the NSF Petascale Simulations and Analysis (PetaApps) program, Grant No. 0749140; the Army Research Laboratory under cooperative agreement number W911NF-12-2-0023; an anonymous gift from Rensselaer and CSIR-National Chemical Laboratory, Pune (India) MLP project Grant No. 028626. Computing resources of the Computational Center for Nanotechnology Innovations (CCNI) at Rensselaer, partly funded by the State of New York, have been used for this work.

Author contributions

C.S.R., D.J.L. and S.K.N. designed experiment. C.S.R., P.D.J., R.V.K. carried out experiment. A.J.S. performed computational calculation. C.S.R., D.S.J., M.A.M., M.W., S.K.N. and D.J.L. carried out data analysis and co-wrote the manuscript. All authors reviewed the manuscript.

Additional information

Supplementary information accompanies this paper at <http://www.nature.com/scientificreports>

Competing financial interests: The authors declare no competing financial interests.

How to cite this article: Rout, C.S. *et al.* Superior Field Emission Properties of Layered WS₂-RGO Nanocomposites. *Sci. Rep.* **3**, 3282; DOI:10.1038/srep03282 (2013).



This work is licensed under a Creative Commons Attribution 3.0 Unported license. To view a copy of this license, visit <http://creativecommons.org/licenses/by/3.0>